Wildfire Progression Time Series Mapping With Interferometric Synthetic Aperture Radar (InSAR)

Roger J. Michaelides, *Member, IEEE*, Matthew R. Siegfried, *Member, IEEE*, Jonathan Lovekin, Karen Berry, Brandon Dugan, and Danica L. Roth

***Abstract*— We describe a novel algorithm to accurately characterize burned area and generate a time series of active burned areal extent during an actively burning wildfire based upon changes in the second-order statistics of interferometric synthetic aperture radar (InSAR) phase measurements. We present this algorithm and demonstrate its use with Sentinel-1 InSAR data collected during the 2020 Cameron Peak Fire, which burned along the Front Range in Colorado, USA. We show that this algorithm can successfully discriminate recently burned and actively burning areas within a fire zone from unburned areas at high spatial resolution (∼10 s of m). We further introduce a method for estimating a time series of burned areal extent from interferometric observations of burned area-change via a singular value decomposition (SVD) inversion. We compare the results of our algorithm with fire progression maps from the National Interagency Fire Center (NIFC) and find good agreement on the total burned area (IoU = 0.65) and excellent agreement on burned area extent (mIoU = 0.91).**

***Index Terms*— Fire monitoring, interferometric synthetic aperture radar (InSAR), radar, remote sensing, time series, wildfire.**

I. Introduction

THE Cameron Peak Fire, which initiated on August 13, 2020, and was contained by December 2, 2020, burned over 208 000 acres across several counties in northern Colorado, USA, making it the largest wildfire in Colorado history [1]. As the frequency and severity of catastrophic wildfire seasons are expected to increase across much of the western United States [2], there is a critical demand for near real-time monitoring of fire severity and evolution to protect life and property as well as minimize damage through effective wildfire emergency response.

Wildfire-burned areas have historically been monitored through a variety of methods, including airborne remote sensing platforms [3] and spaceborne remote sensing platforms [4]. Spaceborne remote sensing platforms afford extensive geographic coverage (in many cases near-global coverage) with relatively frequent (e.g., subdaily to monthly) temporal repeats at modest to fine spatial resolutions; this operational resolution can be augmented by tasking of federal or commercial assets to achieve higher frequency sampling when needed. Spaceborne remote sensing methods are thus particularly well-suited toward identification and time series monitoring of natural hazards at the regional scale. Optical and multispectral remote sensing instruments are commonly employed for near real-time monitoring of wildfires, but these methods are only operable during daytime and are severely limited by cloud cover and smoke columns from active fires (Fig. 1; [5]).

Synthetic aperture radar (SAR), by contrast, is an active radar imaging technique that penetrates clouds, operates in day or night conditions, and provides images at consistent temporal repeats in the microwave spectrum. Previous work has shown that both polarimetric observables and SAR backscatter are sensitive to wildfire burn severity and have been exploited to map total wildfire burned area [6], [7]. Interferometric synthetic aperture radar (InSAR) coherence has been used previously to characterize wildfire burn severity [8], [9]. However, to our knowledge, no work to date has shown that InSAR phase measurements can be directly used for real-time wildfire identification, burned area classification, or wildfire progression monitoring.

In this letter, we demonstrate that second-order statistical interferometric phase information can be used to quantify wildfire burned areal extent and discriminate between active burn and unburned or extinct burn areas within an active fire scar. In this letter, we use "active" to refer to surfaces exhibiting a marked change in surface scattering properties, which we interpret as indicative of recent burn. By contrast, "inactive" refers to surfaces that were interpreted as burning at some point during the observational record, but no longer exhibit evidence for active modification of surface scattering properties. We demonstrate that the second moment of the interferometric phase can outperform coherence thresholding-based methods of feature identification in certain scenarios. Using a singular value decomposition (SVD) inversion approach, we generate a time series of active burned areal extent from InSAR observations, which largely reproduces independently derived fire progression maps from the National Interagency Fire Center (NIFC).

II. Methods

We used Sentinel-1 SAR imagery for all analysis, which we chose due to the broad imaging swath and fine temporal

Manuscript received 3 July 2023; revised 19 January 2024; accepted 8 February 2024. Date of publication 13 February 2024; date of current version 22 February 2024. This work was supported in part by the Colorado Geological Survey and in part by NASA under Grant 80NSSC22K1105. *(Corresponding author: Roger J. Michaelides.)*

Roger J. Michaelides is with the Department of Earth and Planetary Sciences, Washington University in St. Louis, St. Louis, MO 63130 USA (e-mail: roger.michaelides@wustl.edu).

Matthew R. Siegfried and Brandon Dugan are with the Department of Geophysics, Colorado School of Mines, Golden, CO 80401 USA.

Jonathan Lovekin and Karen Berry are with Colorado Geological Survey, Golden, CO 80401 USA.

Danica L. Roth is with the Department of Geology and Geological Engineering, Colorado School of Mines, Golden, CO 80401 USA.

Digital Object Identifier 10.1109/LGRS.2024.3365994

resolution of the Sentinel-1 constellation. This constellation of satellites provides near-global (to ±81.5° latitude) spaceborne SAR coverage of the Earth's surface with 12-day temporal repeats for individual satellites. The use of both ascending and descending tracks results in an effective repeat time of four or eight days. We used Sentinel-1 SAR imagery in interferometric wide (IW) swath mode, in which the C-band (5.405 GHz, 0.056 m wavelength) imaging radars acquired data across a 250 km swath at 5 × 20 m single-look spatial resolution. We processed 11 descending track (path 56, frame 454) and 12 ascending track (path 78, frame 128) SAR images acquired in IW Swath mode by the Sentinel-1 A and B satellites between July 17, 2020 and December 12, 2020, spanning the time period of the Cameron Peak fire.

A. Interferogram Generation

Raw (L1.0) level SAR products were processed using the geocoded single-look complex backprojection method [10] and coregistered to a 5 × 5 m resolution upsampled digital elevation model (DEM) acquired by the Shuttle Radar Topography Mission (SRTM). We then formed a network of interferograms with a maximum temporal baseline of 36 days and a perpendicular baseline of 150 m as in [11] and restricted our analysis to interferograms that spanned the active period of the Cameron Peak Fire. During interferogram formation we performed incoherent averaging by a factor of 3 in both range and azimuth, resulting in interferograms with a final resolution of 15 × 15 m. We unwrapped all interferograms using the SNAPHU algorithm [12] and rejected interferograms exhibiting obvious interferometric decorrelation and/or atmospheric phase noise, which yielded a final total of 13 descending-track and 18 ascending-track interferograms.

B. Burned Area-Change Identification Algorithm

Our newly designed algorithm exploits the observation that the systematic reorientation of surface scatterers—due to, for example, a wildfire burning off a fraction of vegetation cover—leads to interferometric decorrelation. This decorrelation consequently increases the second statistical moment of the observed interferometric phase between two SAR scenes spanning a systematically decorrelative event. Before estimating this change in the second moment of the interferometric phase, we empirically removed the topographically correlated atmospheric phase term from each interferogram as in [13]. To empirically estimate the second statistical moment of the interferometric phase for each interferogram pair, we calculated the local spatial standard deviation of unwrapped phase by convolving each interferogram with a 1 × 1 km standard deviation filter. This approach implicitly assumes that the interferometric phase is ergodic over the spatial scale of the convolutional filter. As a representative example, the interferometric coherence, unwrapped interferometric phase, and phase standard deviation for the August 14, 2020, and September 7, 2020, interferometric pair are shown in Fig. 1.

After estimating the local phase standard deviation, all pixels exhibiting a phase standard deviation above a pre-determined threshold are classified as burned, whereas pixels below this threshold are classified as unburned or not actively burning. As a simple threshold, we chose $\pi/\sqrt{3}$, which is the upper-bound standard deviation for wrapped interferometric phase as the interferometric coherence approaches zero based on the probability density function of the multilook interferometric phase [14]. This threshold value was chosen to minimize the incidence of false positive detections of burned area. This thresholding results in a binary image of pixels classified as burned or unburned. To minimize false positives that arise from spurious decorrelation signals, we performed an area opening operation on the binary image, during which we filtered out all connected components with a total area less than 1 km^2. The steps of the burned area-change identification algorithm are summarized below.

1) Empirically remove the atmospheric phase term correlated with topography as in [13].
2) Convolve each interferogram with a 1 × 1 km standard deviation filter.
3) Classify all pixels exhibiting a phase standard deviation above a pre-determined threshold as burned: $\sigma > (\pi/\sqrt{3})$.
4) Perform area opening operation, removing all connected component regions with a total area less than 1 km^2.

Application of this algorithm yields a set of images with areal estimates of burned-area change—that is, changes in the spatial extent of burned area between the two acquisition times of the SAR scenes used for interferogram generation. To convert this network of area change estimates into a time series estimate of burned areal extent and wildfire progression, we performed a modified form of the Small BAseline Subset (SBAS) time series inversion algorithm described below.

C. Time Series of Burned Area

The (SBAS) algorithm was originally formulated as an inverse problem to generate a time series of surface deformations from a network of interferometric surface-change estimates via an SVD inversion [11]. We can form an analogous linear system of equations that relates the interferometric burned-area change estimates derived in Section II-B to a time series of burned area estimates. For any single burned area-change image acquired between times t_1 and t_2, all nonzero pixels represent a surface element that experienced wildfire burn at some time between times t_1 and t_2. For a collection of N interferograms spanning M discrete observational times, we can construct a pixelwise linear system of N equations of the form

$$\delta\mathbf{a} = \mathbf{B}\mathbf{a} \tag{1}$$

where δ $\mathbf{a}$ is an $[N \times 1]$ vector of burned-area change estimates, $\mathbf{a}$ is an $[M \times 1]$ vector of unknown burned-area estimates, and $\mathbf{B}$ is an $[N \times M]$ incidence-like design matrix whose elements are either 0 or ±1. For example, if the 12th burned-area change image spanned the 5th and 8th observational times, the design matrix would be of the form: $\mathbf{B}(12, 5) = -1$, $\mathbf{B}(12, 8) = 1$. This design matrix is identical for each pixel spanning the series of images, although the vectors $\delta\mathbf{a}$ and $\mathbf{a}$ uniquely encode the time series of burned-area change estimates and burned-area estimates respectively for each pixel. In adapting this proposed method

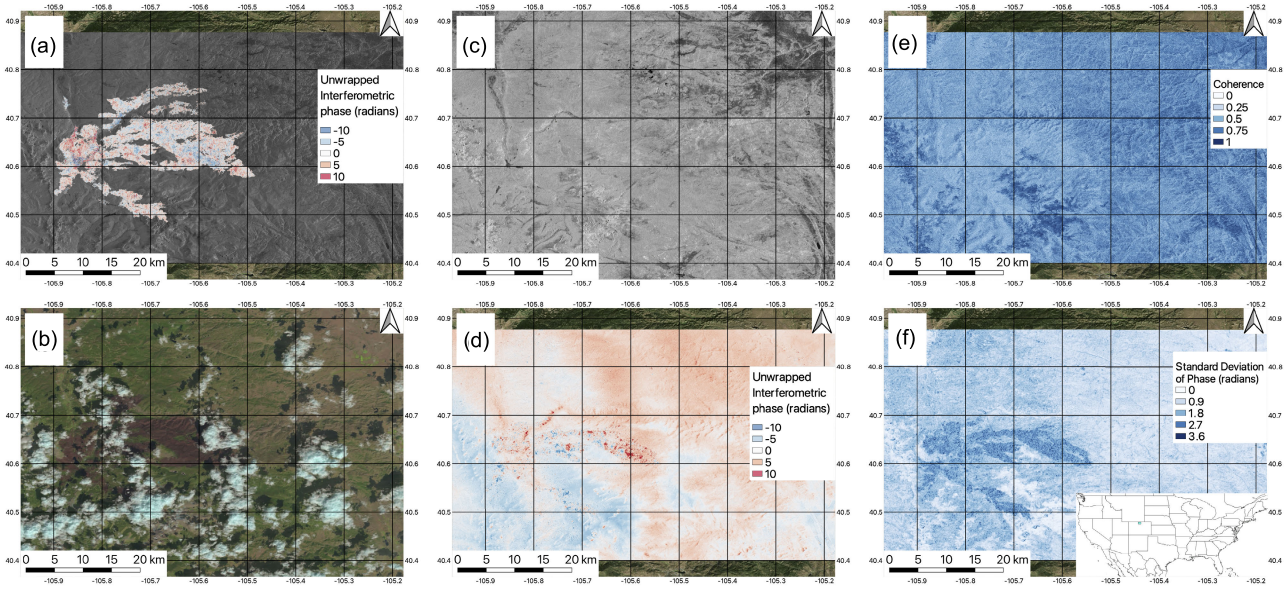

Fig. 1. (a) Unwrapped phase overlying an SAR amplitude image acquired during the 2020 Cameron Peak wildfire, with the burned area as identified via the algorithm described in Section II-B denoted. (b) Contemporaneous Landsat-8 image with the burned area partially obscured with cloud cover, by which SAR is largely unaffected. (c) SAR VV amplitude from September 7, 2020. (d) Unwrapped interferometric phase. (e) Interferometric coherence. (f) Spatial standard deviation of unwrapped interferometric phase over a 1 × 1 km moving window for a pair of SAR scenes from August 14, 2020, and September 7, 2020.

to study active wildfire burn progression in real-time, the design matrix in (1) would need to be updated after each SAR image acquisition; consequently estimates of burned area at a particular time step will progressively improve as more SAR scenes are acquired later in time. The vector of unknown burned area estimates $\mathbf{a}$ can be solved for

$$\mathbf{a} = \mathbf{B}^{-g}\delta\mathbf{a} \tag{2}$$

where $\mathbf{B}^{-g}$ is the generalized inverse of the matrix $\mathbf{B}$. For ease of implementation, we have chosen to use the Moore-Penrose pseudo-inverse of the design matrix $\mathbf{B}$. As a final step to remove spurious pixels, we perform a weighted threshold filtering on the vector of burned-area estimates $\mathbf{a}$, which identifies pixels that are consistently labeled as positive burn pixels for every interferometric observation that spans a particular time step. We define the threshold value ζ_i for the ith burned area time step $\mathbf{a}_i$ as

$$\zeta_i = \frac{1}{P\|\mathbf{B}_i\|^2} \tag{3}$$

where P is an integer scaling factor that can be chosen based on the overall quality of data, and $\|\mathbf{B}_i\|^2$ is the squared Euclidean norm of the ith column in the design matrix $\mathbf{B}$. Each pixel in the array $\mathbf{a}_i$ that is greater than ζ_i is considered a burned pixel; pixels less than ζ_i are considered unburned and masked. We chose $P = 1$ for ascending scenes and $P = 4$ for descending scenes as these resulted in time series with a minimum of spurious signals.

III. Results

Applying the wildfire identification algorithm presented in Section II-B on all 31 ascending and descending track interferograms resulted in 31 burned-area change estimates spanning 12 unique time steps. Solving (2) and performing the weighted thresholding with (3) yielded a time series of 12 burned area estimates from which we can create a progression map of the 2020 Cameron Peak Fire.

TABLE I
IoU and mIoU Results for InSAR-Derived and NIFC Burned Area Estimates

Date	**14 Aug.**	**26 Aug.**	**03 Sep.**	**07 Sep.**	**15 Sep.**	**19 Sep.**
IoU	0.213	0.599	0.662	0.698	0.676	0.758
mIoU	0.968	0.951	0.908	0.887	0.914	0.915
Date	**27 Sep.**	**01 Oct.**	**09 Oct.**	**21 Oct.**	**06 Nov.**	
IoU	0.712	0.727	0.715	0.676	0.692	
mIoU	0.908	0.907	0.859	0.907	0.899	

As shown in Fig. 2, the burned area time series derived from InSAR observations successfully captured the evolution of the fire from its original initiation near Red Feather Lakes through its spread into the Arapaho and Roosevelt National Forests. The InSAR-derived burned area estimates (Fig. 2, white pixels) agreed well with independently derived optical and infrared estimates of burned area provided by the NIFC (Fig. 2, pink pixels). The spatial correlation between the InSAR-derived and optical/infrared-derived burned area estimates was consistently high at each resolved time step. Notably, the InSAR-derived estimates also identify unburned islands contained within the fire perimeter, suggesting that InSAR observations might afford complementary high resolution estimates of heterogenous burn conditions within active fire perimeters. To quantify the agreement between the InSAR-derived areas and the NIFC results, we performed an Intersection-over-Union (IoU) analysis between the two results and a modified IoU (mIoU) analysis (see Table I). The mIoU excludes from the union set pixels contained within the NIFC perimeters but not identified by InSAR, and is therefore most sensitive to differences between the two fire perimeters of each product rather than differences in unburned islands within the

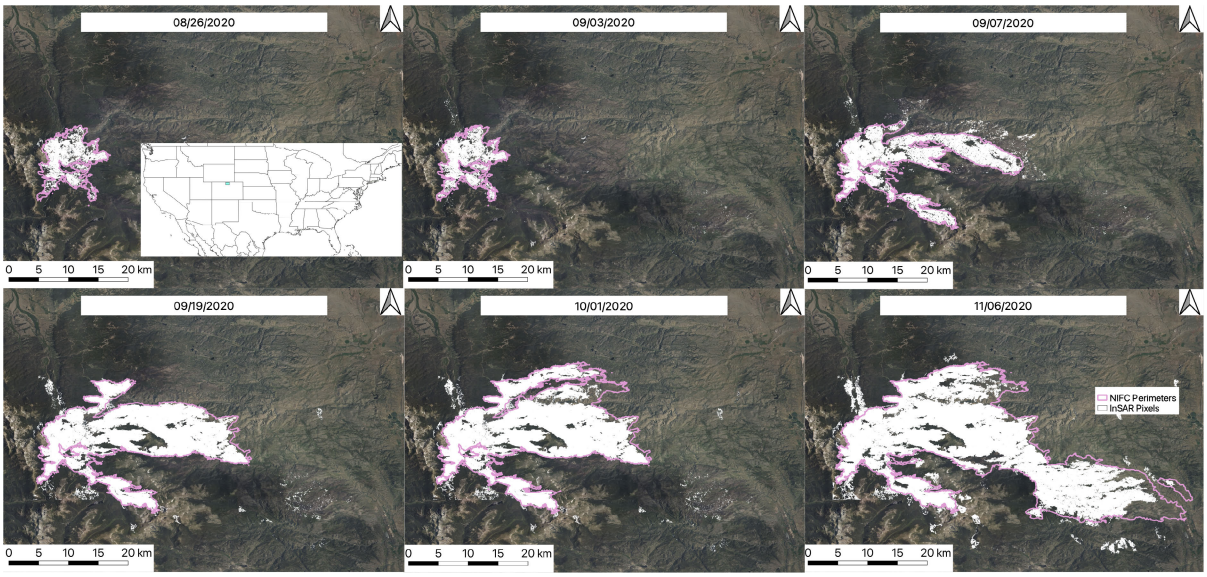

Fig. 2. Selected time steps from the burned area time series of the Cameron Peak Fire (white pixels) as determined by the InSAR algorithm described in Sections II-B and II-C, compared to independent burned-area fire perimeters provided by the (NIFC; pink pixels).

fire perimeters. We use the mIoU score to assess agreement on burned area extent. A value of one indicates a perfect match between InSAR-derived areas and NIFC results, while a value of 0 indicates no agreement. Generally, a value greater than 0.7 is considered a good match, while a value greater than 0.92 is considered an excellent match.

IV. Discussion

Several advantages of our second-order phase-based approach to map fire progression are illustrated in Fig. 1: the all-day, all-weather operating conditions of radar make SAR observations insensitive to variable cloud cover and smoke during active burn conditions, unlike optical methods; the use of interferometric observables (e.g., differential phase) rather than amplitude circumvents issues associated with multiplicative speckle noise [15]; the use of second-order differential phase information rather than first-order differential phase also removes any potential sensitivity to variable propagation phase delay due to uncompensated atmospheric phase and/or propagation through dense smoke columns [16].

Because this method makes use of both ascending and descending tracks, systematic differences in viewing geometry and line of sight of the imaging platform can result in variable image quality. In the case presented here, descending track interferometric pairs exhibited higher interferometric coherence overall and yielded fewer false positives; see, for example, spurious estimates of burned area from ascending-track interferograms in dates October 9, 2020 and October 21, 2020 to the east of the main fire complex in Fig. 2. We attribute the higher fidelity of the descending track interferograms in part due to the favorable viewing geometry of the descending track compared to the ascending track. The Sentinel-1 constellation of satellites is right-looking, which means that the look direction in the descending track is more conducive to imaging the eastern flank of the Colorado Rocky Mountains, where the Cameron Peak Fire occurred. The launch of the left-looking NISAR mission in early 2024 will provide complementary coverage to the right-looking Sentinel-1 constellation of satellites. Furthermore, NISAR will operate with a 1.2575 GHz center frequency, making NISAR observations less sensitive to signal decorrelation [17]. Radiometric terrain flattening approaches might further be employed to improve performance in topographically complex areas [18].

Although changes in interferometric coherence have been previously used to detect total burned area extent of wildfires, these approaches can fail over areas that exhibit generally poor coherence or for individual interferometric pairs exhibiting low coherence. This fact is illustrated in Fig. 1, which shows interferometric observables from an interferometric pair spanning August 14, 2020 and September 7, 2020. The uniformly low coherence over most of the forested study region precludes a simple coherence-thresholding approach for burned area identification. Furthermore, a conventional approach using SAR amplitude would be unable to quantify the burned area.

However, visual inspection of the unwrapped phase clearly shows an increase in the spatial standard deviation of unwrapped phase within burned pixels as opposed to unburned pixels, even when the interferometric coherence in both areas is comparable. Estimation of the phase standard deviation clearly delineates the burn scar with the borders between burned and unburned ground sharply resolved, in contrast to the interferometric coherence. This difference between the interferometric coherence and the spatial standard deviation of the interferometric phase is due both to the different spatial domain of the coherence estimator and phase standard deviation filter, as well as the difference in probability distributions of the two estimated parameters.

Implicit in these results is the simplifying assumption that the algorithm described in Section II-B solely identifies decorrelative events that are entirely due to the effects of wildfire burn. As a result, several false positive pixels are identifiable as spurious, disconnected regions at certain time intervals in Fig. 2. These false positives might be correctable through the

incorporation of ancillary datasets (e.g., multispectral-derived burned-area estimates [5]) or more stringent filtering choices, such as convolving the standard deviation filter over a larger area, performing image opening over a larger threshold area, or a different integer scaling factor in (3). Conversely, the fact that this algorithm relies only on interferometric observables means that it is in principle generalizable to study other physical phenomena that are responsible for systematic interferometric decorrelation, such as extreme precipitation events [19], forest disturbance [20], agricultural activities [21], changes in soil moisture [22], and snow accumulation [23]. For example, the greater discrepancy between the InSAR-derived results and the NIFC results in October and November may be partially attributable to increased precipitation events. Future research is warranted to test the applicability of the proposed technique to study other dynamic surface processes.

V. Conclusion

We have introduced a new algorithm that uses second order statistical interferometric phase information from Sentinel-1 InSAR observations to generate burned area-change estimates over the 2020 Cameron Peak Fire. We further introduced a simple SVD-based method to generate a time series of burned area estimates from burned area-change estimates and demonstrated excellent agreement between our results and independent estimates of fire progression from the federal agency tasked with generating burned-area outlines, the NIFC. In contrast to optical and multispectral instruments, SAR instruments have the attractive qualities of operability during day or night conditions, all-weather conditions, and insensitivity to cloud cover or smoke cover during active burn conditions. These results illustrate that InSAR is an effective technique for acquiring fire-synchronous estimates of burned area and can complement existing techniques while providing beneficial insensitivities to atmospheric obscurations.

Acknowledgment

Copernicus Sentinel data was retrieved from Alaska Satellite Facility Distributed Active Archive Center, processed by the European Space Agency. Independent daily burned acreage estimates were provided by the NIFCs 2020 National Incident Feature Service Archive tables, accessed on 08/15/22. Our code is freely available at https://github.com/rmich342/insar-wildfire-timeseries.

References

[1] M. Caggiano, T. Beeton, B. Gannon, and J. White, "The Cameron peak fire: Use of potential operational delineations and risk management assistance products," in *Proc. CFRI*, 2021, pp. 1–16.

[2] A. L. Westerling, "Increasing western U.S. forest wildfire activity: Sensitivity to changes in the timing of spring," *Phil. Trans. Roy. Soc. B, Biol. Sci.*, vol. 371, no. 1696, Jun. 2016, Art. no. 20150178.

[3] S. N. Hirsch, "Airborne infrared mapping of forest fires," *Fire Technol.*, vol. 1, no. 4, pp. 288–294, Nov. 1965.

[4] L. L. Bourgeau-Chavez, P. A. Harrell, E. S. Kasischke, and N. H. F. French, "The detection and mapping of Alaskan wildfires using a spaceborne imaging radar system," *Int. J. Remote Sens.*, vol. 18, no. 2, pp. 355–373, Jan. 1997.

[5] S. Veraverbeke et al., "Hyperspectral remote sensing of fire: State-of-the-art and future perspectives," *Remote Sens. Environ.*, vol. 216, pp. 105–121, Oct. 2018.

[6] K. Czuchlewski and J. Weissel, "Synthetic aperture radar (SAR)-based mapping of wildfire burn severity and recovery," in *Proc. IEEE Int. Geosci. Remote Sens. Symp. (IGARSS)*, vol. 1, 2005, p. 4.

[7] Y. Ban, P. Zhang, A. Nascetti, A. R. Bevington, and M. A. Wulder, "Near real-time wildfire progression monitoring with Sentinel-1 SAR time series and deep learning," *Sci. Rep.*, vol. 10, no. 1, p. 1322, Jan. 2020.

[8] S. Takeuchi and S. Yamada, "Monitoring of forest fire damage by using JERS-1 InSAR," in *Proc. IEEE Int. Geosci. Remote Sens. Symp.*, Jun. 2002, pp. 3290–3292.

[9] R. Rykhus and Z. Lu, "Monitoring a boreal wildfire using multi-temporal Radarsat-1 intensity and coherence images," *Geomatics, Natural Hazards Risk*, vol. 2, no. 1, pp. 15–32, Mar. 2011.

[10] Y. Zheng and H. A. Zebker, "Phase correction of single-look complex radar images for user-friendly efficient interferogram formation," *IEEE J. Sel. Topics Appl. Earth Observ. Remote Sens.*, vol. 10, no. 6, pp. 2694–2701, Jun. 2017.

[11] P. Berardino, G. Fornaro, R. Lanari, and E. Sansosti, "A new algorithm for surface deformation monitoring based on small baseline differential SAR interferograms," *IEEE Trans. Geosci. Remote Sens.*, vol. 40, no. 11, pp. 2375–2383, Nov. 2002.

[12] C. W. Chen and H. A. Zebker, "Two-dimensional phase unwrapping with use of statistical models for cost functions in nonlinear optimization," *J. Opt. Soc. Amer. A, Opt. Image Sci.*, vol. 18, no. 2, p. 338, Feb. 2001.

[13] H. Zebker, "Accuracy of a model-free algorithm for temporal InSAR tropospheric correction," *Remote Sens.*, vol. 13, no. 3, p. 409, Jan. 2021.

[14] J.-S. Lee, K. W. Hoppel, S. A. Mango, and A. R. Miller, "Intensity and phase statistics of multilook polarimetric and interferometric SAR imagery," *IEEE Trans. Geosci. Remote Sens.*, vol. 32, no. 5, pp. 1017–1028, Mar. 1994.

[15] M. A. Belenguer-Plomer, M. A. Tanase, A. Fernandez-Carrillo, and E. Chuvieco, "Burned area detection and mapping using Sentinel-1 backscatter coefficient and thermal anomalies," *Remote Sens. Environ.*, vol. 233, Nov. 2019, Art. no. 111345.

[16] F. Onn and H. A. Zebker, "Correction for interferometric synthetic aperture radar atmospheric phase artifacts using time series of zenith wet delay observations from a GPS network," *J. Geophys. Res., Solid Earth*, vol. 111, no. B9, Sep. 2006, Art. no. B09102.

[17] H. A. Zebker and J. Villasenor, "Decorrelation in interferometric radar echoes," *IEEE Trans. Geosci. Remote Sens.*, vol. 30, no. 5, pp. 950–959, Sep. 1992.

[18] D. Small, "Flattening gamma: Radiometric terrain correction for SAR imagery," *IEEE Trans. Geosci. Remote Sens.*, vol. 49, no. 8, pp. 3081–3093, Aug. 2011.

[19] C. P. Scott, R. B. Lohman, and T. E. Jordan, "InSAR constraints on soil moisture evolution after the March 2015 extreme precipitation event in Chile," *Sci. Rep.*, vol. 7, no. 1, p. 4903, Jul. 2017.

[20] P. M. Bürgi and R. B. Lohman, "Impact of forest disturbance on InSAR surface displacement time series," *IEEE Trans. Geosci. Remote Sens.*, vol. 59, no. 1, pp. 128–138, Jan. 2021.

[21] R. J. Michaelides, H. A. Zebker, and Y. Zheng, "An algorithm for estimating and correcting decorrelation phase from InSAR data using closure phase triplets," *IEEE Trans. Geosci. Remote Sens.*, vol. 57, no. 12, pp. 10390–10397, Dec. 2019.

[22] M. Nolan, D. R. Fatland, and L. Hinzman, "DInSAR measurement of soil moisture," *IEEE Trans. Geosci. Remote Sens.*, vol. 41, no. 12, pp. 2802–2813, Dec. 2003.

[23] S. Oveisgharan and H. A. Zebker, "Estimating snow accumulation from InSAR correlation observations," *IEEE Trans. Geosci. Remote Sens.*, vol. 45, no. 1, pp. 10–20, Jan. 2007.